CILIA AND FLAGELLA

In situ architecture of the ciliary base reveals the stepwise assembly of intraflagellar transport trains

Hugo van den Hoek[1,2,3]†, Nikolai Klena[4,5]†, Mareike A. Jordan[6], Gonzalo Alvarez Viar[5,6], Ricardo D. Righetto[1,2], Miroslava Schaffer[3], Philipp S. Erdmann[5], William Wan[7], Stefan Geimer[8], Jürgen M. Plitzko[3], Wolfgang Baumeister[3], Gaia Pigino[5,6]*, Virginie Hamel[4]*, Paul Guichard[4]*, Benjamin D. Engel[1,2]*

The cilium is an antenna-like organelle that performs numerous cellular functions, including motility, sensing, and signaling. The base of the cilium contains a selective barrier that regulates the entry of large intraflagellar transport (IFT) trains, which carry cargo proteins required for ciliary assembly and maintenance. However, the native architecture of the ciliary base and the process of IFT train assembly remain unresolved. In this work, we used in situ cryo–electron tomography to reveal native structures of the transition zone region and assembling IFT trains at the ciliary base in *Chlamydomonas*. We combined this direct cellular visualization with ultrastructure expansion microscopy to describe the front-to-back stepwise assembly of IFT trains: IFT-B forms the backbone, onto which bind IFT-A, dynein-1b, and finally kinesin-2 before entry into the cilium.

Cilia (and closely related flagella) are evolutionarily conserved eukaryotic organelles that extend from the cell surface and are involved in a wide variety of functions, including cell motility, fluid flow generation, sensing, and signaling (*1*, *2*). The cilium consists of an axoneme of microtubule doublets (MTDs), which extend from the microtubule triplets (MTTs) of the centriole (also called a basal body) and are sheathed in a ciliary membrane. At the base of the cilium, a specialized region known as the transition zone (TZ) gates entry and exit of both membrane-bound and soluble ciliary proteins (*3*–*5*). Among its many gating functions, the TZ is believed to regulate entry of intraflagellar transport (IFT), bidirectional traffic between the ciliary base and tip driven by kinesin and dynein motors (*6*, *7*). IFT is required for assembly and maintenance of the cilium, as well as for mediating many of its signaling functions (*8*). A pool of IFT proteins and motors resides at the ciliary base for several seconds before entry into the cilium (*9*, *10*). However, it remains to be characterized how these proteins assemble into the elaborate multi-megadalton IFT trains observed running along the ciliary axoneme (*11*). In this study, we combined in situ cryo–electron tomography (cryo-ET) (*12*) with ultrastructure expansion microscopy (U-ExM) (*13*) of the green alga *Chlamydomonas reinhardtii*, a classic model for cilia research, to reveal native TZ structures and stepwise assembly of IFT trains at the ciliary base.

Vitrified *Chlamydomonas* cells were thinned with a focused ion beam (FIB) (*14*) then imaged by cryo-ET, revealing the ciliary base inside the native cellular environment (figs. S1 and S2). Focusing on the TZ, we observed several different structures attached to the MTDs (Fig. 1, A and B), which we resolved in molecular detail by subtomogram averaging (Fig. 1, C to H, and figs. S3 and S4). The proximal ~180 nm of the TZ is occupied by peripheral Y-links (Fig. 1, turquoise) and luminal stellate fibers (Fig. 1, purple, and fig. S2), which resemble a nine-pointed star in cross section (*15*). Our structure reveals that the stellates form a helical cylinder with a six-start helix and a pitch of 49.2 nm (Fig. 1H). Notably, this matches the pitch of the inner scaffold, a three-start helical cylinder in the lumen of the centriole (*16*). The nine points of the stellate star bind MTDs at protofilament A3, with a longitudinal periodicity of ~8.1 nm along each MTD (Fig. 1F and fig. S5), which matches the 8.2 nm length of one tubulin dimer.

Y-links are present in many species. They connect MTDs to the ciliary membrane and help gate transport into and out of the cilium (*17*–*20*). Our structure reveals a broad density attaching the Y-links to the MTD, spanning protofilaments A9, A10, and B1 to B4, with a longitudinal repeat of ~8.3 nm (Fig. 1F and fig. S5). However, the outer densities of the Y-links that connect to the ciliary membrane were not resolved, likely owing to flexibility of these filamentous structures. We observed that the Y-links extend along the MTDs proximal of the ciliary membrane (Fig. 1A). This suggests that connection to the membrane is not a prerequisite for MTD Y-link decoration.

Immediately distal to the stellates and Y-links, we found a distinct helical density completely decorating the MTDs (Fig. 1, dark blue). This helical "sleeve" spans 76 ± 6 nm along the MTDs, with a periodicity of ~16.4 nm (fig. S5). Cryo-ET and U-ExM immediately after ciliary shedding (figs. S6 and S7) revealed that the MTD sleeve overlaps with the ciliary cleavage site, also known as the site of flagellar autotomy (SOFA) (*21*) (Fig. 1B). Consistent with this finding, the MTD sleeve was absent from the severed ends of MTDs both on the TZ (fig. S6, C and D) and isolated cilia (*22*). We therefore hypothesize that this structure might help regulate axoneme severing and is lost during the process. Because the sleeve density covers every MTD protofilament, it should sterically hinder the attachment of molecular motors and thus may also play a role in regulating IFT entry or exit. The sleeve does not appear to be present on the TZ of motile cilia from bovine trachea (*23*).

It has been known for decades that a pool of IFT proteins is localized near the base of the cilium (*24*, *25*), but the structural organization of this basal pool has remained a mystery. In our tomograms, we observed filamentous strings of particles with one end attached to the TZ and the other end splayed into the cytosol, passing between the transition fibers (Fig. 2A and fig. S8). These strings consisted of three layers, each with a different shape and periodicity (Fig. 2, B and C, and fig. S9). We performed subtomogram averaging of particles along each layer and combined them to produce a composite molecular structure (Fig. 2D and fig. S10). Comparison to a previously published cryo-ET structure of mature anterograde IFT trains within the cilium (*11*) confirmed that the cytosolic strings are indeed IFT trains. Our observed cytosolic train structure was similar to the anterograde train structure (fig. S11), enabling us to assign densities to IFT-B complexes, IFT-A complexes, and dynein-1b motors, which have longitudinal periodicities of ~6, ~11, and ~18 nm, respectively (fig. S12). As was shown for anterograde IFT, we observed that these cytosolic trains were attached to the MTD B-tubule (fig. S13D) (*26*) and that dynein-1b was loaded onto the trains as a cargo in an autoinhibited state (*11*, *27*). Thus, much of the IFT pool at the ciliary base consists of TZ-tethered anterograde IFT trains that are undergoing assembly before entry into the cilium. We did not see retrograde trains at the ciliary base, which implies that they rapidly disassemble, perhaps even before exiting the TZ.

We observed two notable differences between assembling and mature IFT trains. First, assembling trains are flexible and display regions of high curvature (Fig. 2, A to C, and fig. S9), whereas trains in the cilium have an extended straight conformation (fig. S12) (*11*),

[1]Biozentrum, University of Basel, 4056 Basel, Switzerland. [2]Helmholtz Pioneer Campus, Helmholtz Munich, 85764 Neuherberg, Germany. [3]Department of Molecular Structural Biology, Max Planck Institute of Biochemistry, 82152 Martinsried, Germany. [4]Department of Molecular and Cellular Biology, Section of Biology, University of Geneva, 1211 Geneva, Switzerland. [5]Human Technopole, 20157 Milan, Italy. [6]Max Planck Institute of Molecular Cell Biology and Genetics, 01307 Dresden, Germany. [7]Department of Biochemistry and Center for Structural Biology, Vanderbilt University, Nashville, TN 37232, USA. [8]Cell Biology and Electron Microscopy, University of Bayreuth, 95447 Bayreuth, Germany.
***Corresponding author. Email: gaia.pigino@fht.org (G.P.); virginie.hamel@unige.ch (V.H.); paul.guichard@unige.ch (P.G.); ben.engel@unibas.ch (B.D.E.)**
†These authors contributed equally to this work.

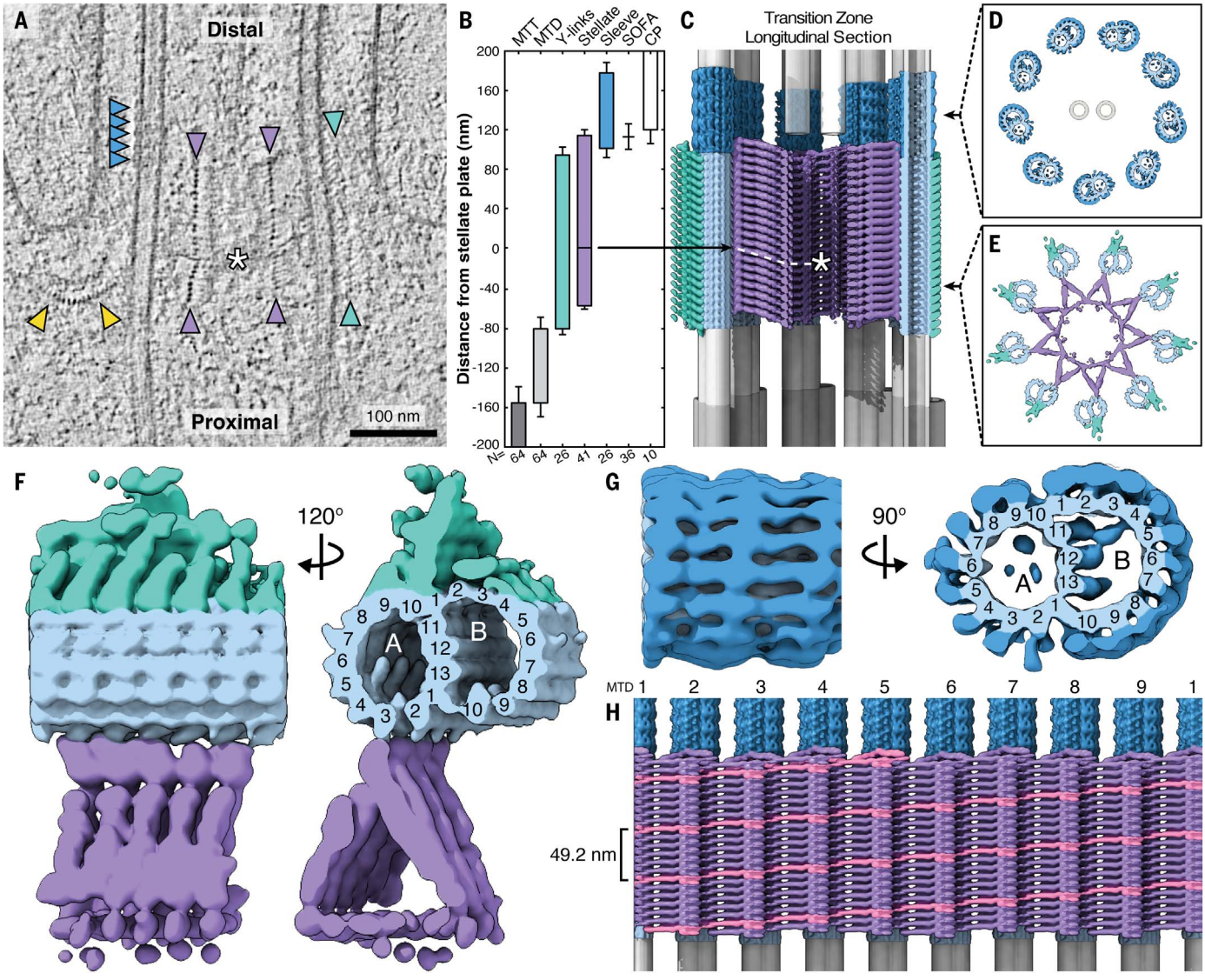

Fig. 1. Cryo-ET structure of the ciliary transition zone within native *Chlamydomonas* cells. (**A**) 2D slice through a cryo–electron tomogram, showing a TZ in longitudinal cross section. Stellate fibers, purple; Y-links, turquoise; MTD helical sleeve, dark blue; stellate plate, white asterisk (see fig. S2); and IFT, yellow (see Fig. 2). Scale bar: 100 nm. (**B**) Position along the TZ occupied by different structures. Distances are measured relative to the stellate plate (see fig. S6), defined as the "0 nm" origin point. SOFA, site of flagellar autotomy, where the cilium is cleaved (see figs. S6 and S7). CP, central pair. Error bars indicate standard deviation. (**C** to **E**) Composite model of the TZ, combining averages of the stellate (purple), Y-links (turquoise), MTD sleeve (dark blue), and associated MTD (light blue), with schematic renderings of MTTs (dark gray), MTDs (light gray), and the CP (white). (C) Longitudinal section view of the complete composite model, assembled according to the measured lengths and positions of each component, with 21 Y-link repeats, 21 stellate repeats (7 proximal of the plate, 14 distal), and 5 MTD sleeve repeats. The model shows straight MTTs and MTDs, but, as seen in (A) and quantified in (*16*), the centriole is actually a slightly convex barrel. [(D) and (E)] Cross-sectional views through the indicated regions of the composite model, showing (D) MTDs encased in the helical sleeve, with the CP in the middle, and (E) the nine-pointed stellate cylinder attached to MTDs decorated with Y-links. (**F** and **G**) Side and cross-sectional views of a single MTD attached to (F) stellate fibers and Y-links and (G) the helical sleeve. Protofilaments of the A- and B-microtubules are numbered. (**H**) Unrolled composite model, viewed from the center of the TZ, looking outward toward the inner wall of the stellate cylinder. One continuous helical density of the six-start stellate helix is marked in pink (pitch: 49.2 nm). MTDs are numbered. See also movie S1.

which is likely maintained by interactions with cargos and the ciliary membrane. Second, assembling IFT-B has a prominent extra density on the side opposite IFT-A (Fig. 2D and fig. S11; red asterisks). In regions where IFT trains are bound to the TZ, this extra density is positioned adjacent to the MTD. The density is not part of the MTD structure itself, because it is also present on IFT-B in the sections of trains that dangle into the cytosol (fig. S13).

In situ cryo-ET combines native molecular structures with precise cellular localization, enabling us to plot the spatial relationship between assembling IFT trains and the TZ (Fig. 3, A and B). The front segments of IFT trains attach to MTDs (but never to the MTTs of the centriole) and then continue in the distal direction along these microtubule tracks, while the back regions curve away from the TZ into the cytosol. The front ends of IFT trains were frequently observed at the Y-links, but only very rarely further distal at the MTD sleeve (fig. S9). By mapping the IFT-B, IFT-A, and dynein-1b structures along the IFT trains

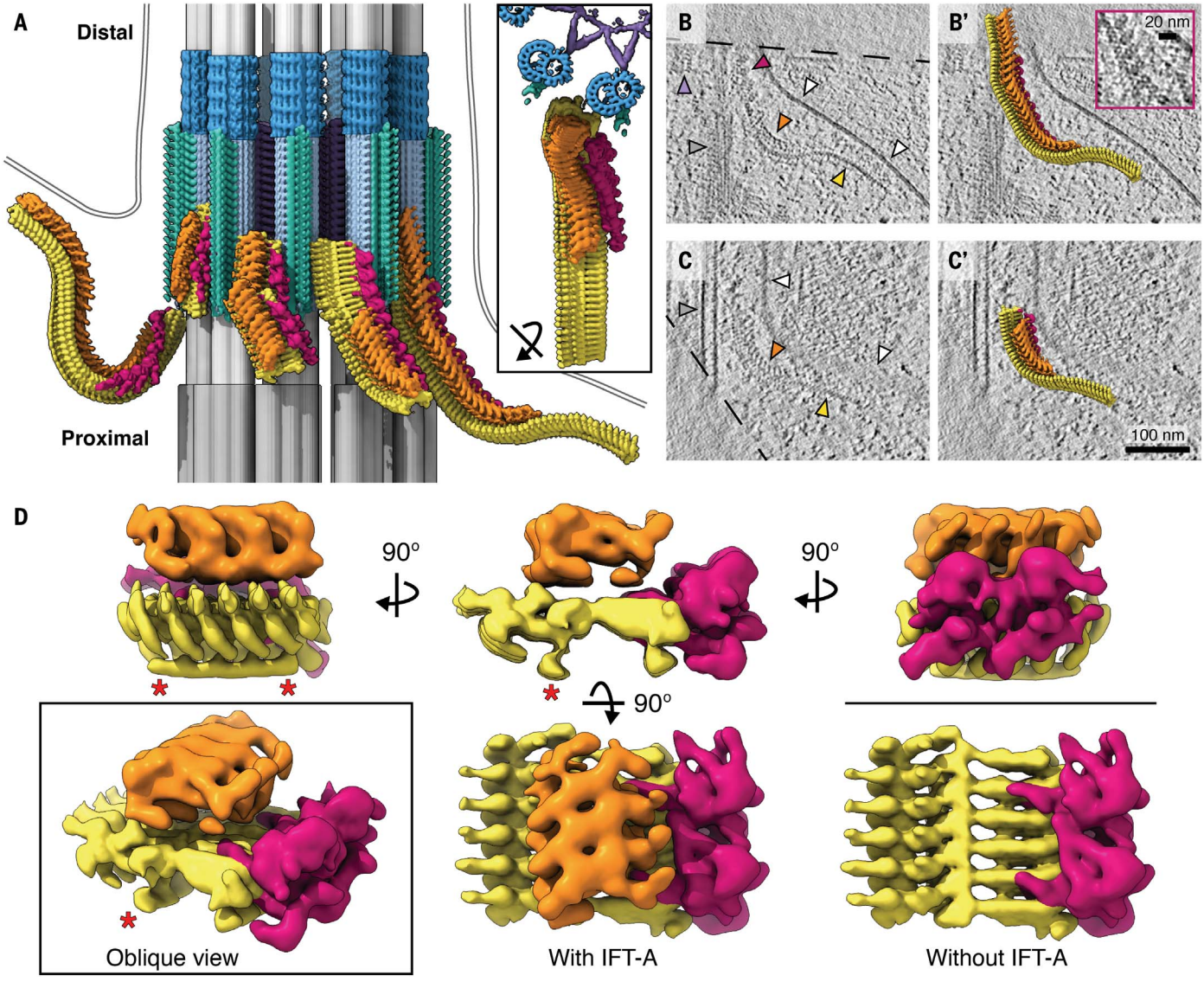

Fig. 2. Cryo-ET structures of assembling IFT trains attached to the transition zone. (**A**) Composite structures of assembling IFT trains (IFT-B, yellow; IFT-A, orange; and dynein-1b, red) engaging the ciliary TZ (colored as in Fig. 1). A schematic membrane has been added (gray double lines). Subtomogram averages have been mapped back into their positions inside a representative tomogram. (Inset) Rotated top view of the rightmost IFT train from (A). (**B** and **C**) 2D slices through tomograms, showing assembling IFT trains, and (**B′** and **C′**) overlaid 3D train structures, with their front ends attached to the TZ. (Inset) Enlarged view showing the double AAA+ adenosine triphosphatase rings of the dynein-1b motors. Arrowhead colors correspond to (A): MTT/MTD, gray, and membrane, white. Scale bars: 100 nm in (B) and (C), 20 nm in the inset. (**D**) Different views of the cytosolic IFT train composite subtomogram average. Colored as in (A). In the lower right, IFT-A was removed to show details on IFT-B. Red asterisks indicate the extra IFT-B density, which was not observed on mature trains inside cilia (see fig. S11). Assembling trains were only found attached to the TZ, not in the surrounding cytosol farther from the ciliary base (see fig. S1). See also movie S2.

(as shown in Fig. 2A), we visualized the spatially defined order of train assembly. Anterograde trains always contain IFT-B, which forms a backbone scaffold upon which other components are attached. This train architecture is consistent with previous findings that IFT-B recruits IFT-A into cilia (*28*, *29*). We plotted the train assembly state relative to each IFT-B subunit, and although we observed variability between individual trains (Fig. 3A), the cumulative plot shows a clear distribution of IFT train components (Fig. 3B). The back segments of trains were in a less assembled state, with IFT-B extending the farthest, followed by IFT-A and then dynein-1b (we did note some assembling trains where dynein-1b extended farther than IFT-A). No gaps were observed in the regions occupied by IFT-A and dynein-1b, suggesting that these components linearly oligomerize from front to back on the IFT-B scaffold.

Next, we compared the assembling cytosolic trains to mature anterograde trains within the cilium (Fig. 3, C and D). Mature trains exhibited a continuum of lengths from 223 to 558 nm, comprising 36 to 90 IFT-B subunits with an average of 62 ± 16 IFT-B. In comparison, the longest assembling train we observed contained 88 IFT-B subunits, and the average length was 44 ± 17 IFT-B. Thus, just one IFT train is assembled at a time per MTD. Cytosolic and ciliary IFT trains have similarly incomplete front ends, whereas the incomplete segment at the back of cytosolic trains is longer, as these regions are still undergoing assembly (Fig. 3D). Perhaps as IFT trains enter the cilium, part of the incompletely assembled

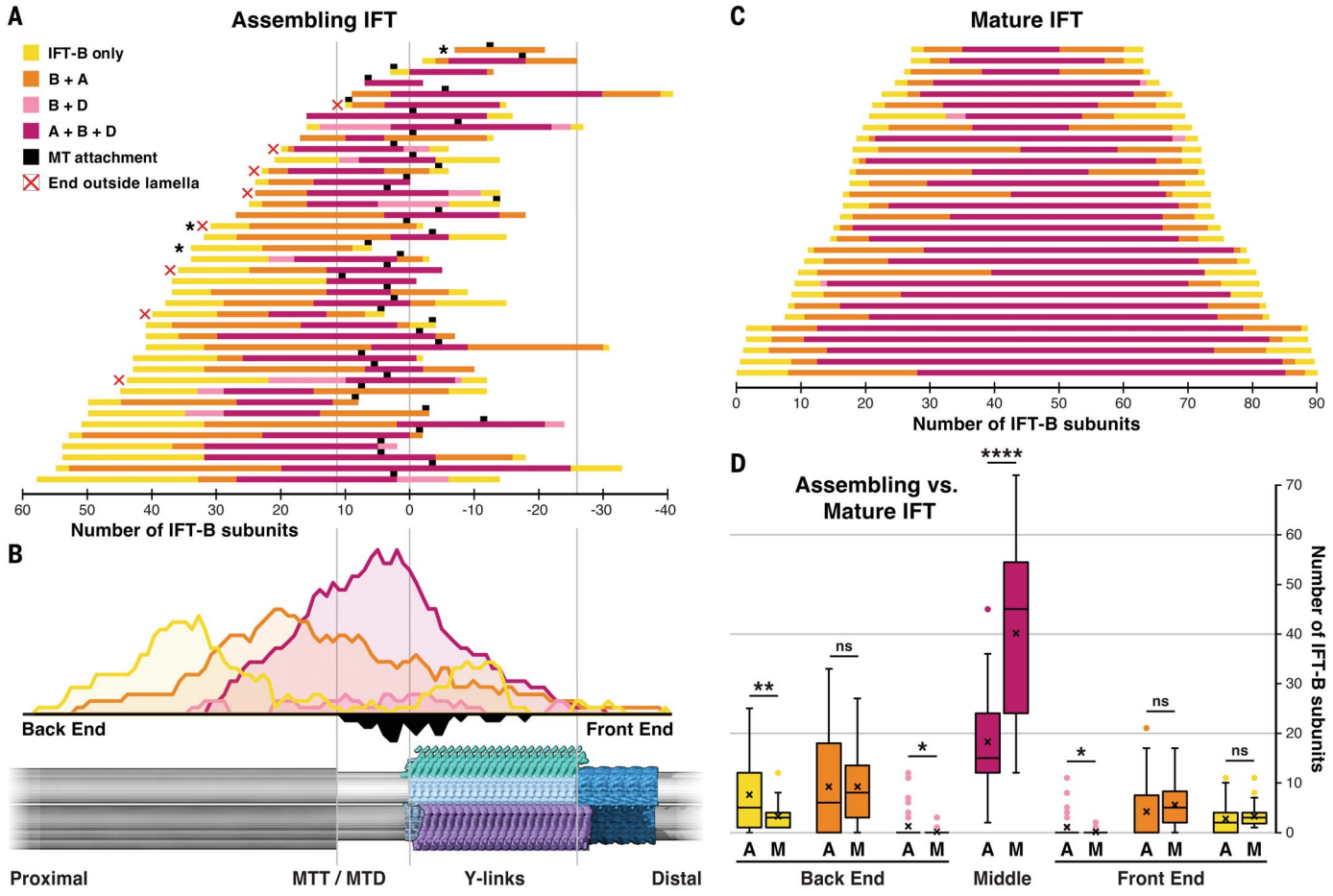

Fig. 3. IFT trains undergo stepwise assembly from front to back. (**A** and **B**) Assembly states of IFT trains relative to structures of the TZ [shown at the bottom of (B)]. Distances are measured by the number of IFT-B subunits relative to the onset of the Y-links (defined as the "0 IFT-B" origin point). (A) Position and train assembly state, measured for each IFT-B subunit of each assembling IFT train. Assembly states [color code in (A) applies to all panels] were determined on the basis of occupancy of IFT-A and/or dynein-1b on the IFT-B backbone. Black squares indicate train attachment points, that is, the most proximal IFT-B subunit that is close enough to the MTD (<20 nm) to be considered bound to the microtubule. The three trains marked with black asterisks lack a complete "middle" (no dynein is bound) and thus were omitted from analysis in (D) because "back-end B + A" could not be split from "front-end B + A." Of the 70 trains in our dataset, 30 had front ends cropped by the FIB milling and therefore were not quantified, as their starting point relative to the TZ could not be determined. Eight more trains had cropped back ends (indicated with a red "x") but were included in the analysis. (B) Cumulative plot of all assembling IFT trains in (A), with positions in relation to the TZ (shown at bottom). Colored curves above the line show the summed abundance of each IFT assembly state. The black curve below the line shows the distribution of MTD attachment points, summed from the black squares in (A). (**C**) Distribution of IFT train lengths and completeness of assembly [colored as in (A)] for mature anterograde trains found in the cilium (*11*). (**D**) Comparison of the abundance of assembly states at the front and back ends of assembling ("A") versus mature ("M") trains [i.e., trains in (A) versus trains in (C)]. Box, median and 25 to 75% percentiles; X, mean; whiskers, 1.5× interquartile range; points, outliers. Statistical significance assessed by unpaired *t* test (****$P < 0.0001$; **$P = 0.002$; *$P = 0.03$; ns, not significant, $P > 0.05$). Because the backs of some assembling trains in this analysis were clipped by the FIB milling ["x" in (A)], the "IFT-B only" region of assembling trains should be slightly more pronounced than the quantification shown here.

back end is left behind at the TZ to nucleate the front of the next train (Fig. 4K). Because assembly of IFT-A and dynein-1b proceeds front to back, the front end of the new train would remain incomplete, as we see in mature anterograde trains inside the cilium (Fig. 3C).

The kinesin-2 anterograde IFT motor is difficult to identify by cryo-ET owing to its relatively small size and flexible structure. We thus turned to U-ExM to examine the occupancy of kinesin-2 on assembling trains. We imaged components of kinesin-2, dynein-1b, IFT-B (subcomplexes B1 and B2), and IFT-A (Fig. 4, A to G, and fig. S14). Consistent with our cryo-ET data, all of these proteins formed filamentous strings at the ciliary base, with their distal ends in close proximity to the TZ (marked by centrin staining and the lack of glutamylated tubulin) (figs. S15 and S16) and their proximal ends curving into the cytoplasm. Using semiautomated tracing, we plotted the three-dimensional (3D) trajectories of each protein (fig. S15E). IFT-B traces were longer than traces of IFT-A and dynein-1b (Fig. 4H). Kinesin-2 traces were the shortest and were localized at the front of IFT trains close to the TZ (fig. S16). Double-labeling of individual IFT trains confirmed that IFT-A extends farther than kinesin-2 toward the back of the train, and IFT-B extends farther than IFT-A (Fig. 4, I and J, and fig. S17).

We observed ninefold occupancy of IFT around the majority of TZs (Fig. 4, F and G, and fig. S18). Measured by U-ExM, cryo-ExM, and cryo-ET, 93 to 96% of MTDs were bound by an assembling IFT train. Given that trains enter the cilium with a frequency of ~1 train/s (*28*, *30*), we predict that trains linger at the ciliary base for an average of 9 s during

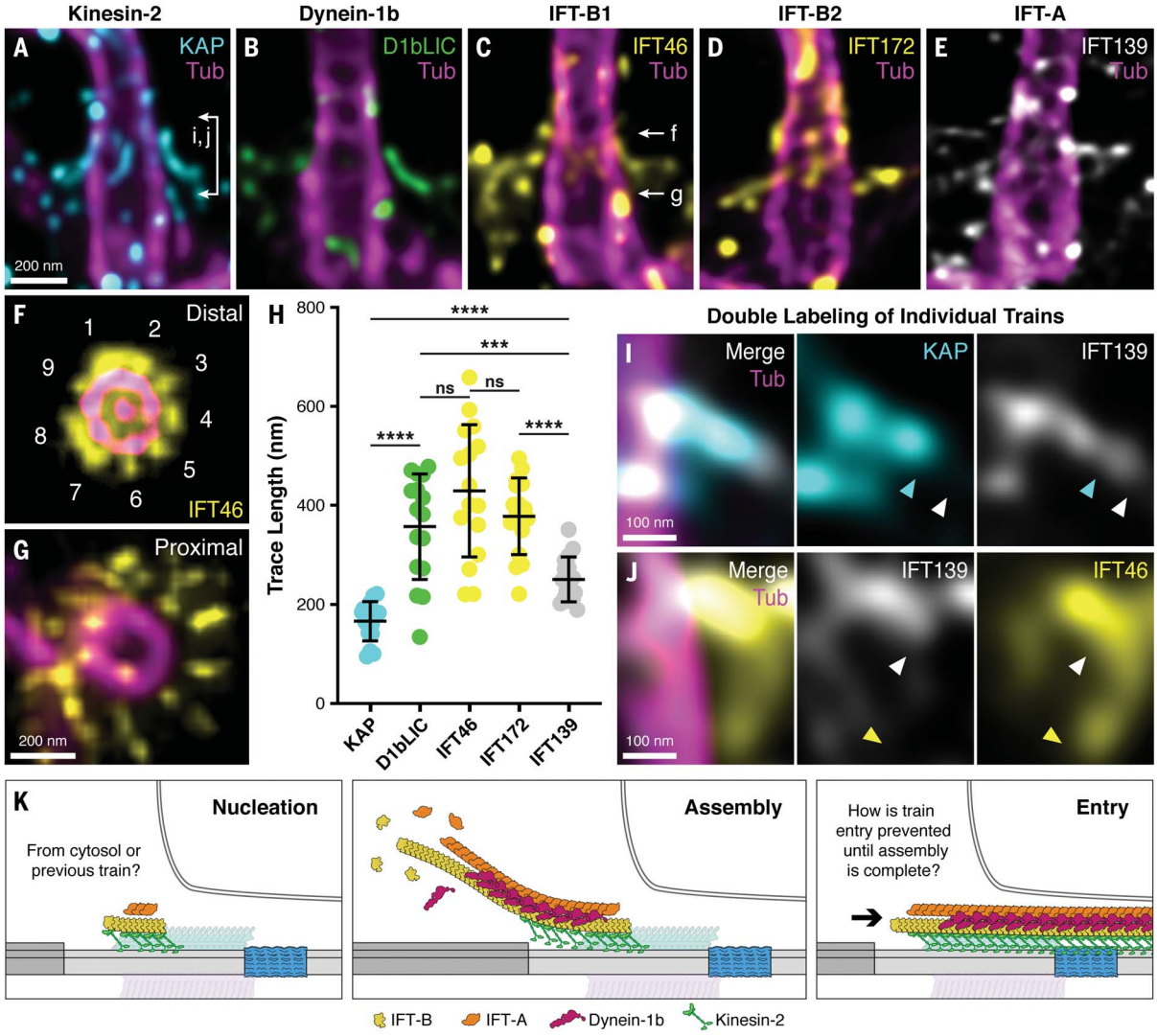

Fig. 4. Assembly of anterograde IFT trains examined by U-ExM. (**A** to **E**) Longitudinal views of assembling IFT trains at the ciliary base, visualized by antibody staining and U-ExM. (A) KAP-GFP (cyan). Connected arrows mark the approximate region shown in (I) and (J). (B) D1bLIC-GFP (green). (C) IFT46-YFP (yellow). White arrows indicate approximate positions of top views in (F) and (G). (D) IFT72 (yellow). (E) IFT139 (gray). Tubulin staining is magenta. (**F** and **G**) Top views displaying ninefold occupancy of IFT trains at (F) the distal TZ (confirmed by the presence of the central pair) and (G) the proximal TZ (see fig. S18). (**H**) Measured lengths of 3D traces for each IFT component on the assembling trains (see fig. S15E). Statistical significance assessed by unpaired *t* test (****P < 0.0001; ***P = 0.0009; ns, not significant, P > 0.05). U-ExM length trends are consistent with cryo-ET (Fig. 3), except that D1bLIC traces were longer than IFT139. One possible explanation could be that IFT139 is added to trains after the rest of IFT-A, but these short traces might also be influenced by a weaker anti-IFT139 antibody (see methods). (**I** and **J**) Dual staining of IFT trains at the TZ for (I) KAP + IFT139 and (J) IFT46 + IFT139. Arrowheads indicate the back ends of each IFT component on the train (see fig. S17). (**K**) Consensus model of IFT train assembly from cryo-ET and U-ExM measurements. New IFT-B subunits are added to the back of the train, forming a scaffold that is loaded with IFT-A, dynein-1b, and finally kinesin-2 close to the TZ. Z-projection thickness: 0.24 μm in (A) to (F), (I) and (J), 0.36 μm in (G). Scale bars: 200 nm in (A) to (G), 100 nm in (I) and (J).

assembly. Consistent with this hypothesis, photobleaching analysis of the *Chlamydomonas* basal pool showed that several green fluorescent protein (GFP)–tagged IFT proteins require ~9 s to recover peak fluorescence (*9*). Regardless, ciliary entry appears to be stochastic rather than sequential, with an avalanche-like relationship between lag time and IFT train size (*31*).

Our combined cryo-ET and U-ExM measurements support a spatially defined sequence of IFT train assembly: IFT-B first forms the backbone, which scaffolds the front-to-back attachment of IFT-A, dynein-1b, and finally kinesin-2 close to the TZ (Fig. 4K). A major remaining question is how IFT entry into the cilium is regulated. What prevents the front end of the train from entering the cilium as assembly proceeds toward the incomplete back of the train? Possible mechanisms may include controlled loading of kinesin-2 by factors at the TZ, the sleeve serving as a barrier to prevent entry of small trains, or the extra IFT-B–associated density acting as a molecular brake until train assembly is completed.

REFERENCES AND NOTES

1. M. V. Nachury, D. U. Mick, *Nat. Rev. Mol. Cell Biol.* **20**, 389–405 (2019).
2. D. R. Mitchell, *Cold Spring Harb. Perspect. Biol.* **9**, a028290 (2017).
3. Q. Hu *et al.*, *Science* **329**, 436–439 (2010).
4. H. L. Kee *et al.*, *Nat. Cell Biol.* **14**, 431–437 (2012).
5. D. K. Breslow, E. F. Koslover, F. Seydel, A. J. Spakowitz, M. V. Nachury, *J. Cell Biol.* **203**, 129–147 (2013).
6. G. Pigino, *Curr. Biol.* **31**, R530–R536 (2021).

7. K. G. Kozminski, K. A. Johnson, P. Forscher, J. L. Rosenbaum, *Proc. Natl. Acad. Sci. U.S.A.* **90**, 5519–5523 (1993).
8. H. Ishikawa, W. F. Marshall, *Nat. Rev. Mol. Cell Biol.* **12**, 222–234 (2011).
9. J. L. Wingfield *et al.*, *eLife* **6**, e26609 (2017).
10. J. V. K. Hibbard, N. Vazquez, R. Satija, J. B. Wallingford, *Mol. Biol. Cell* **32**, 1171–1180 (2021).
11. M. A. Jordan, D. R. Diener, L. Stepanek, G. Pigino, *Nat. Cell Biol.* **20**, 1250–1255 (2018).
12. S. Asano, B. D. Engel, W. Baumeister, *J. Mol. Biol.* **428**, 332–343 (2016).
13. D. Gambarotto *et al.*, *Nat. Methods* **16**, 71–74 (2019).
14. M. Schaffer *et al.*, *J. Struct. Biol.* **197**, 73–82 (2017).
15. S. Geimer, M. Melkonian, *J. Cell Sci.* **117**, 2663–2674 (2004).
16. M. Le Guennec *et al.*, *Sci. Adv.* **6**, eaaz4137 (2020).
17. B. Craige *et al.*, *J. Cell Biol.* **190**, 927–940 (2010).
18. C. L. Williams *et al.*, *J. Cell Biol.* **192**, 1023–1041 (2011).
19. F. R. Garcia-Gonzalo, J. F. Reiter, *Cold Spring Harb. Perspect. Biol.* **9**, a028134 (2017).
20. A. R. G. De-Castro *et al.*, *J. Cell Biol.* **221**, e202010178 (2022).
21. L. M. Quarmby, in *The Chlamydomonas Sourcebook* (*Second Edition*), *Volume 3*, E. H. Harris, D. B. Stern, G. B. Witman, Eds. (Academic Press, 2009), pp. 43–69.
22. K. H. Bui, T. Yagi, R. Yamamoto, R. Kamiya, T. Ishikawa, *J. Cell Biol.* **198**, 913–925 (2012).
23. G. A. Greenan, R. D. Vale, D. A. Agard, *J. Cell Biol.* **219**, e201907060 (2020).
24. D. G. Cole *et al.*, *J. Cell Biol.* **141**, 993–1008 (1998).
25. Y. Hou *et al.*, *J. Cell Biol.* **176**, 653–665 (2007).
26. L. Stepanek, G. Pigino, *Science* **352**, 721–724 (2016).
27. K. Toropova *et al.*, *Nat. Struct. Mol. Biol.* **26**, 823–829 (2019).
28. C. Iomini, V. Babaev-Khaimov, M. Sassaroli, G. Piperno, *J. Cell Biol.* **153**, 13–24 (2001).
29. J. M. Brown, D. A. Cochran, B. Craige, T. Kubo, G. B. Witman, *Curr. Biol.* **25**, 1583–1593 (2015).
30. B. D. Engel, W. B. Ludington, W. F. Marshall, *J. Cell Biol.* **187**, 81–89 (2009).
31. W. B. Ludington, K. A. Wemmer, K. F. Lechtreck, G. B. Witman, W. F. Marshall, *Proc. Natl. Acad. Sci. U.S.A.* **110**, 3925–3930 (2013).

ACKNOWLEDGMENTS

We thank T. Ishikawa, A. Noga, D. Diener, and K. Lechtreck for helpful discussions that influenced the manuscript. G.P. and G.A.V. thank T. Furstenhaupt from the MPI-DBG EM facility for instrument support. Calculations were performed at the Max Planck Institute for Biochemistry computing cluster in Martinsried, Germany, and at the sciCORE (https://scicore.unibas.ch/) scientific computing center at the University of Basel. **Funding:** This work was funded by the European Research Council (ERC) under the European Union's Horizon 2020 research and innovation program (grant 819826) to G.P., the Swiss National Science Foundation (SNSF) Grant PP00P3_187198 to P.G., the ERC ACCENT Starting Grant 715289 to P.G., a European Molecular Biology Organization (EMBO) Fellowship (grant ALTF 537–2021) to N.K., and an Alexander von Humboldt Foundation Fellowship to R.D.R. (R.D.R. also acknowledges a nonstipendiary fellowship from EMBO). Additional funding for personnel and instrumentation was provided by Helmholtz Munich, the Max Planck Society, and the Biozentrum of the University of Basel. **Author contributions:** M.S., P.S.E., and B.D.E. acquired cryo-ET data of FIB-milled *C. reinhardtii* cells. G.A.V. prepared samples and acquired cryo-ET data of isolated basal bodies. M.A.J. prepared samples and acquired cryo-ET data of intact cilia. H.v.d.H. analyzed all the cryo-ET data, with help from M.A.J., R.D.R., and W.W. U-ExM data acquisition and analysis was performed by N.K., with guidance from P.G. and V.H. Conventional electron microscopy was performed by S.G. Additional mentorship was provided by W.B. and J.M.P., along with access to instrumentation. G.P., V.H., P.G., and B.D.E. initiated and supervised the study. H.v.d.H., N.K., and B.D.E. wrote the paper, with input from all authors. **Competing interests:** W.B. is on the life science advisory board of Thermo Fisher. **Data and materials availability:** Cellular tomograms, subtomogram averages, and composite maps have been deposited at the Electron Microscopy Data Bank (EMD-15252 to EMD-15263, see table S2). Raw cryo-ET data are available from the Electron Microscopy Public Image Archive (EMPIAR-11078). All data needed to evaluate the conclusions of the study are present in the paper and the supplementary materials. Correspondence and requests for materials should be addressed to B.D.E. (ben.engel@unibas.ch).

SUPPLEMENTARY MATERIALS

science.org/doi/10.1126/science.abm6704
Materials and Methods
Figs. S1 to S18
Tables S1 and S2
References (*32*–*64*)
MDAR Reproducibility Checklist
Movies S1 and S2

View/request a protocol for this paper from *Bio-protocol*.

Submitted 3 October 2021; accepted 27 June 2022
10.1126/science.abm6704

Science

In situ architecture of the ciliary base reveals the stepwise assembly of intraflagellar transport trains

Hugo van den HoekNikolai KlenaMareike A. JordanGonzalo Alvarez ViarRicardo D. RighettoMiroslava SchafferPhilipp S. ErdmannWilliam WanStefan GeimerJürgen M. PlitzkoWolfgang BaumeisterGaia PiginoVirginie HamelPaul GuichardBenjamin D. Engel

Science, 377 (6605), • DOI: 10.1126/science.abm6704

Close-up view of transport train assembly

Cilia and flagella extend from the cell surface of various eukaryotic cells and perform diverse motility and signaling functions. The base of the cilium controls the entry of large intraflagellar transport trains that carry important cargo proteins throughout this specialized organelle. Defects in the ciliary base result in altered ciliary composition and human diseases. van den Hoek *et al*. used a combination of cryo–electron tomography and expansion microscopy techniques to study the molecular architecture of the ciliary base in the green alga *Chlamydomonas reinhardtii*. Their findings elucidate how intraflagellar transport trains assemble before they enter cilia and demonstrate the possibility of visualizing dynamic events with molecular resolution inside native cells. —SMH

Science (ISSN) is published by the American Association for the Advancement of Science. 1200 New York Avenue NW, Washington, DC 20005. The title *Science* is a registered trademark of AAAS.